Chapter 4

Effect of Fiber Waviness on Tensile Properties of Sliver-Based Natural Fiber Composites

Taweesak Piyatuchsananon, Baosheng Ren and Koichi Goda

Additional information is available at the end of the chapter

http://dx.doi.org/10.5772/intechopen.70905

Abstract

Glass and carbon fiber-reinforced composite materials have been applied for the high demand in industrial use to date, because their advantages are light weight, high strength, and corrosion resistance. However, the disposal problem after the use of these materials has also surfaced as a serious environmental problem. As a measure to solve this problem, many researchers have tried to investigate the potential of plant-based natural fibers instead of artificial fibers. When we use natural fibers as a long fiber-reinforcement, the negative point is *irregular* fiber waviness inherent in a sliver form. This is because such fiber waviness often decreases the mechanical properties. The purpose of this study is thus to clarify the relation between irregular fiber waviness and the composite's tensile strength. The clarification was performed from two points of view: One is quantification of irregular fiber waviness, based on *spatial analysis* such as Local Moran's *I* and Geary's *c*. Result shows that quantified parameters were correlated well with tensile strengths of sliver-based natural fiber composites. Another is a 3-D finite element analysis in which the fiber waviness was treated as an orthotropic body. Finally, the relation of the tensile strengths with maximum stress and Tsai-Hill criterions was discussed.

Keywords: plant-based natural fiber, fiber waviness, spatial analysis, tensile strength, finite element method, failure criterion

1. Introduction

To date, fiber-reinforced composite materials have been used in many industries such as automotive and aerospace, because their advantages are high strength and low specific gravity. Especially, carbon and glass fibers are typical reinforcements of the composite materials.

On the other hand, it is known that production of these fibers needs a large quantity of electric energy [1]. After the use of glass fiber composites, as is also known, serious environmental problems have been caused at the process of disposal [2, 3]. Although several recycle techniques have been developed for used glass fiber composites [3, 4], scientists and engineers have tried to use plant-based natural fibers such as flax, kenaf, curaua, and ramie, which are environmentally friendly materials as an alternative [5–9]. Composite materials reinforced with the natural fibers are a nonexpensive and fast-growing material, and therefore expected to replace in whole or partially artificial fibers. Materials composed of natural fibers and biodegradable or thermoplastic resin are often called "green composites," and have been applied for car interiors [10]. Normally, automotive makers often apply short fiber composites to their interior or exterior parts, which are produced by injection molding, but mechanical properties of short fiber composites are less than long fiber composites. However, there is a problem in the usage of long fiber, which is *fiber waviness* that reduces the stiffness and strength [9]. Hsiao and Daniel [11] explored the relation between fiber waviness and mechanical properties, and proposed a theoretical model of elastic constants on a unidirectional carbon/epoxy composite with fiber waviness by the assumption of sine function. The shape of waviness by sine function was also developed by numerical analysis method [12, 13]. The results show that the ratio of amplitudes denoted as waviness parameter has an effect on the mechanical properties. Allison and Evans [14] inserted a single waviness part in a unidirectional composite and discussed its strength by identifying its wavy shape as a notch. Karami and Garnich [12] applied a failure criterion to a laminate in which a fiber wavy layer is included, using a finite element analysis. As a key-point in these papers, the fiber wavy shape was all given as a sinusoid [15]. On the other hand, the effect of *irregular* fiber waviness on tensile strength has also been studied. Ren et al. [16, 17] used Pearson's type of one- and two-dimensional autocorrelation to analyze the randomness in fiber waviness of a curaua- and flax sliver-reinforced composite, respectively. However, this method does not necessarily classify local size and intensity in irregular fiber waviness, which has the tendency to give risky areas on specimen.

Thus, the first purpose of this study is to evaluate quantitatively the randomness in fiber waviness of a flax sliver-reinforced composite, based on the *spatial analysis* such as Local Moran's I and Local Geary's c [18]. Such analyses are known as an effective method to evaluate spatial autocorrelation of point patterns, of which the object in this study is a fiber orientation angle in a small segment on the composite specimen surface. The analyzed autocorrelation value is recognized as an intensity of fiber waviness on each segment. Finally, we discuss if total size of the high intensity segments, so-called *area ratio*, affects the tensile strength of a flax sliver-reinforced composite or not.

The second purpose of this study is to explore the effect of the fiber waviness on a flax sliver-reinforced composite strength, using three-dimensional finite element analysis (3-D FEA). An orthotropic body was assumed for each finite element, which is corresponding to above-mentioned each segment. Through major stress components, maximum stress and reduced Tsai-Hill criterions [19] were applied for the prediction of risky areas in the composite. Results show that these criterions can predict the degree of damage for each element, but are not a decisive factor inducing the composite fracture. It was estimated that, finally, the specimen was fractured by mechanical unbalance in tensile stress distribution between laminae, brought from irregular fiber waviness.

http://dx.doi.org/10.5772/intechopen.70905

2. Experimental and analysis methods

2.1. Material preparation

To prepare the composite specimen, a flax sliver (TEIKOK SEN-I Co., Ltd.) was used as a reinforcement and shown in **Figure 1(a)**. A biodegradable resin (Randy PL-1000; Miyoshi Oil and Fat Co. Ltd., Japan) was used as a matrix resin in **Figure 1(b)**. This resin was supplied in a water emulsion containing micro-order fine particles of approximately 5.0 μm diameter. The Randy PL-1000 is made from plant-derived resins. Some physical and mechanical properties were shown in **Table 1**.

2.2. Production method and the measurement of fiber orientation angle

In this research, two preparation methods were used to clarify the difference between the composites without and with fiber waviness. First method is the sheet laminate method (denoted as SLM) in which the sliver was combed to form unidirectionally oriented fibers before resin pasting. Another method is the direct method (denoted as DM), in which the sliver was used as a supply state. Thus, SLM is a composite without fiber waviness, whereas DM is a composite influenced with fiber waviness.

For the molding process, first, the emulsion type resin was painted on the sliver, and the emulsion-immersed sliver was dried for 24 hours. The semi-material obtained is called the *pre-preg*. Next, the pre-preg was cut into the size 100 × 100 mm, and two pre-pregs were put into the mold in a compression molding machine. The temperature was set at 150°C for 40 min, and the hydraulic pressure was set at 3 MPa. Subsequently, the temperature was reduced to room

Figure 1. Materials used in this study: (a) as-supplied flax sliver and (b) biodegradable resin.

Material	Density (Mg/m^3)	Fiber width (μm)	Tensile strength (MPa)	Fracture strain (%)	Young's modulus (GPa)
Randy PL-1000	1.2	–	32.5	–	3.8
Flax fiber	1.5	10–30	600–1100	1.5–2.4	40–100

Table 1. Properties of the matrix resin and fiber used in this study.

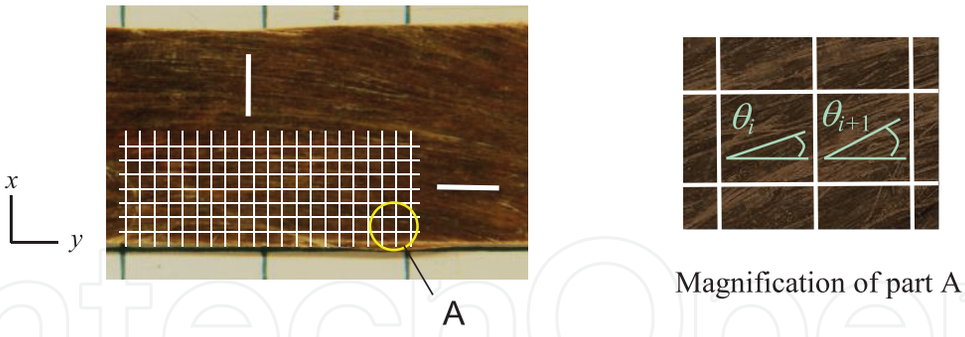

Figure 2. Division into segments on a DM specimen surface.

temperature at 3 MPa pressure for 24 hours. The resultant composite is a laminate consisting of two laminae. The thickness of the laminate is approximately 0.8 mm.

In order to quantify the irregular fiber waviness, fiber orientation angles on the specimen surface were measured by image analysis software (Asahi Kasei Corp., Japan). On the surfaces, y-axis and x-axis were respectively placed along the longitudinal and transverse directions of the specimen. The specimen was divided into small segments of 1.0 × 1.0 mm square size, as shown in **Figure 2**, which are composed of 50 segments along y-axis and 15 segments along x-axis. Thus, the total number of segments is 750 for each surface on the specimen.

2.3. Tensile test of composite specimens with and without fiber waviness

Specimens of DM and SLM composites with the size of 100 × 100 mm square were cut to 15 mm width. Before tensile test, the fiber volume fractions of all composite specimens were calculated as:

$$V_f = 1 - \frac{W - W_f}{\rho_m V} \tag{1}$$

where W is the composite specimen weight, W_f is the flax weight in the composite, V is the composite specimen volume, and ρ_m is the density of the biodegradable resin. After that, aluminum plates were attached with epoxy adhesive to both ends, which shaved 45° for preventing the stress concentration. The shape and dimension is shown in **Figure 3**. The thickness of the specimens was 0.4–0.8 mm. A strain gage was attached on the center of the

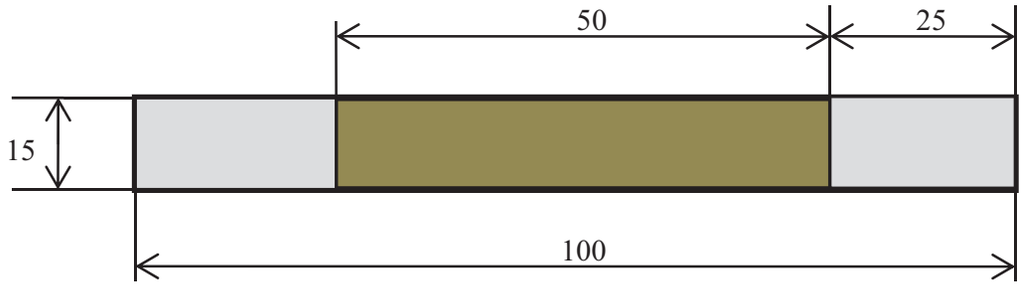

Figure 3. Shape and dimension of the tensile specimen.

specimen surface to measure uniaxial strain. Tensile test was carried out using an Instron-type testing machine (Autograph IS-500; Shimadzu Corp.) at the cross-head speed of 1 mm/min.

When conducting 3-D FEA, as mentioned later, elastic constants are needed. In this study, average Young's modulus and Poisson's ratio of SLM specimens were respectively regarded as the elastic constants, E_2, and Poisson's ratio, ν_{12}. To obtain E_1, SLM specimen with 100 × 100 mm was cut perpendicularly to the fiber axis, and the tensile specimen with 90° direction was produced with the same shape and dimension as **Figure 3**. Regarding E_3, the composite was assumed to be transversely isotropic. In addition to elastic constants, tensile strengths of SLM specimens with 0° and 90° directions were adopted as S_2 and S_1, respectively, and were used for failure criterions in Section 2.6.

2.4. Spatial autocorrelation analysis

Spatial autocorrelation analysis is a statistical tool to interpret the degree of dependence among observations in a space, based on the feature locations and the feature values [18]. From this point of view, the degree of random fiber waviness on DM composite specimen was quantified using two types of spatial autocorrelation analysis methods, Local Moran's *I* and Local Geary's *c*.

2.4.1. Local Moran's I

A spatial measure called Local Moran's *I* was created by P. A. P. Moran [18]. This measure is a typical tool to analyze data point patterns of which the concept is based on a deviation from the average. Local Moran's *I* is given for each segment as:

$$I_i = \frac{\left(\theta_i - \overline{\theta}\right)}{\frac{1}{n}\sum_{i=1}^{n}\left(\theta_i - \overline{\theta}\right)^2} \sum_{\substack{j=1 \\ j \neq i}}^{n} w_{ij}(d)\left(\theta_j - \overline{\theta}\right) \tag{2}$$

where θ_i is the measured angle of *i*-th segment, and $\overline{\theta}$ is the average of all measured angles. $w_{ij}(d)$ is the weight function of the pair samples in distance class *d* at Eq. (3), given as:

$$w_{ij}(d) = \frac{1}{\sqrt{d}} = \frac{1}{\sqrt{\left(x_i - x_j\right)^2 + \left(y_i - y_j\right)^2}} \tag{3}$$

In Eq. (3), *d* is given as a distance between the central positions of *i*-th and *j*-th segments. Hence, x_i and y_i are central positions of *i*-th segment along the *x*-axis and *y*-axis in the ranges of 1–15 mm and 1–50 mm, respectively. From Eqs. (2) and (3), it is understood that I_i (*d*) is more susceptible for segments closer to *i*-th segment. Local Moran's *I* varies between −1 and +1. If Local Moran's *I* approaches +1, then the angle at this location is more largely far from the average, but relatively close to the neighbor's angles in their deviation from the average. On the other hand, if Local Moran's *I* tends to approach −1, then the angle at this location is also higher or lower than the average. In this case, the sign is different from the neighbor angles. When Local Moran's *I* tends to approach 0, the angle at this location is similar to the average.

Theoretically, when Local Moran's *I* is either much higher or lower than 0, then the fiber orientation angle is significantly different from the average. Consequently, such Local Moran's *I* points, if gathered locally, could form a large disordered area in fiber orientation. Hereinafter, Local Moran's *I* is denoted as LM-*I*.

2.4.2. Local Geary's c

Local Geary's *c* is another typical spatial measure, which avoids the effect of average data by using a deviation around *i*-th position. Local Geary's *c* is also given for each segment as:

$$c_i = \frac{1}{\frac{1}{n}\sum_{i=1}^{n}\left(\theta_i - \overline{\theta}\right)^2} \sum_{\substack{j=1 \\ j \neq i}}^{n} w_{ij}(d)\left(\theta_i - \theta_j\right)^2 \tag{4}$$

Local Geary's *c* varies between 0 and 1. When Local Geary's *c* tends to approach 0, the angle at this location is similar to the neighbor angles. In contrast, when Local Geary's *c* tends to approach 1, the angle at this location differs from the sign of neighbor angles or much higher than the neighbor's angles in absolute value. Consequently, such points can be disordered parts in fiber orientation. Local Geary's *c* is hereinafter denoted as LG-*c*.

2.5. Finite element analysis for composite specimen with fiber waviness

To obtain stress distributions on DM specimens, three-dimensional finite element analysis (3-D FEA) was used on Cartesian coordinate system. In this analysis, we assumed that the material was an orthotropic property, of which the stress $\{\sigma\}$–strain $\{\varepsilon\}$ relation was given as follows [20]:

$$\{\boldsymbol{\sigma}\} = \left[T_{ij}\right]^{-1}[C]\left[T'_{ij}\right]\{\boldsymbol{\varepsilon}\},$$

$$[C] = \begin{bmatrix} C_{11} & C_{12} & C_{13} & 0 & 0 & C_{16} \\ C_{12} & C_{22} & C_{23} & 0 & 0 & C_{26} \\ C_{13} & C_{23} & C_{33} & 0 & 0 & C_{36} \\ 0 & 0 & 0 & C_{44} & C_{45} & 0 \\ 0 & 0 & 0 & C_{45} & C_{55} & 0 \\ C_{16} & C_{26} & C_{36} & 0 & 0 & C_{66} \end{bmatrix} \tag{5}$$

where $\{\boldsymbol{\sigma}\} = \{\sigma_x\ \sigma_y\ \sigma_z\ \tau_{yz}\ \tau_{zx}\ \tau_{xy}\}^T$ and $\{\boldsymbol{\varepsilon}\} = \{\varepsilon_x\ \varepsilon_y\ \varepsilon_z\ \gamma_{yz}\ \gamma_{zx}\ \gamma_{xy}\}^T$. $[T_{ij}]$ is the coordinate transformation matrix and $\left[T'_{ij}\right]$ is the transposed matrix of $[T_{ij}]^{-1}$ $(i,\ j = 1, \ldots, 6)$. The components of the stiffness matrix $[C]$ for an orthotropic material in terms of the engineering constants are shown as:

$$C_{11} = \frac{1 - v_{23}v_{32}}{E_2E_3\Delta}, C_{22} = \frac{1 - v_{13}v_{31}}{E_1E_3\Delta}, C_{12} = \frac{v_{21} + v_{31}v_{23}}{E_2E_3\Delta} = \frac{v_{12} + v_{32}v_{13}}{E_1E_3\Delta},$$

$$C_{23} = \frac{v_{32} + v_{12}v_{31}}{E_1E_3\Delta} = \frac{v_{23} + v_{21}v_{13}}{E_1E_2\Delta}, C_{13} = \frac{v_{31} + v_{21}v_{32}}{E_2E_3\Delta} = \frac{v_{13} + v_{12}v_{23}}{E_1E_2\Delta},$$

http://dx.doi.org/10.5772/intechopen.70905

$$C_{33} = \frac{1 - v_{12}v_{21}}{E_1E_2\Delta}, C_{44} = G_{23,}\ C_{55} = G_{31}, C_{66} = G_{12},$$

$$\Delta = \frac{1 - v_{12}v_{21} - v_{23}v_{32} - v_{31}v_{13} - 2v_{21}v_{32}v_{13}}{E_1E_2E_3} \tag{6}$$

where, E is Young's modulus, ν is Poisson's ratio, and G is shear modulus. The fibers are aligned on the 2-axis (on-axis), and 1- and 3-axes are perpendicular to the 2-axis at right angles to each other. When y-axis is placed along the longitudinal direction of the specimen, a fiber alignment has an angle θ to the y-axis on the x-y plane, and the stress components on the fiber axis are changed through $[T_{ij}]$ as follows:

$$\begin{bmatrix} \sigma_1 \\ \sigma_2 \\ \sigma_3 \\ \tau_{23} \\ \tau_{31} \\ \tau_{12} \end{bmatrix} = [T_{ij}] \begin{bmatrix} \sigma_x \\ \sigma_y \\ \sigma_z \\ \tau_{yz} \\ \tau_{zx} \\ \tau_{xy} \end{bmatrix}, \quad [T_{ij}] = \begin{bmatrix} m^2 & n^2 & 0 & 0 & 0 & 2mn \\ n^2 & m^2 & 0 & 0 & 0 & -2mn \\ 0 & 0 & 1 & 0 & 0 & 0 \\ 0 & 0 & 0 & m & -n & 0 \\ 0 & 0 & 0 & n & m & 0 \\ -mn & mn & 0 & 0 & 0 & m^2 - n^2 \end{bmatrix} \tag{7}$$

where $m = \cos\theta$ and $n = \sin\theta$. In this formulation, no inclination of fibers occurs in the z-x plane. Finite element mesh used in this analysis is shown in **Figure 4**, in which then isoparametric

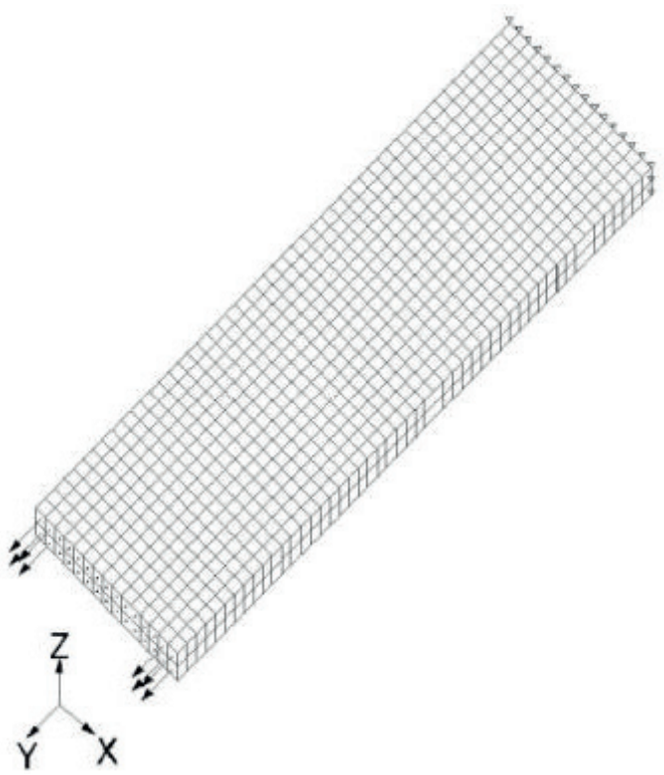

Figure 4. Three-dimensional representation of finite element mesh.

8-node hexahedron element was used. This mesh consists of two laminae, and it is assumed that no delamination occurs during deformation. Thus, each contact point at the interface between the laminae was bonded through one-nodal point. The number of element was 1500, and the number of nodal points was 7344. Each lamina consists of 750 elements, of which the meshing was constructed in the same way as the segments at angle measurement described in Section 2.2. The angle measured in each segment was substituted for θ in Eq. (7).

Elastic constants used here are as follows: when we set the fiber volume faction, V_f, as 0.70, E_1 and E_3 = 3210 MPa, E_2 = 39,500 MPa, ν_{21} and ν_{23} = 0.401, ν_{12} and $\nu_{32} = \nu_{21}E_1/E_2$. These original constants were obtained experimentally, as mentioned in Section 2.3, and estimated to the constant values at V_f = 0.7 through the rule of mixture and Reuss rule. G_{12} and G_{23} = 1610 MPa. These shear moduli was assumed as $E_1/2$ through Ref. [16]. G_{31} was also assumed as being $G_{12}/2$ from Ref. [21].

The boundary condition was a forced displacement, which was applied at one end of the finite element mesh along y-axis. Another end was fixed along y-axis.

2.6. Failure criterion

To evaluate risky area in the composites with fiber waviness, maximum stress and Tsai-Hill failure criterions are applied for the stresses on the specimen.

2.6.1. Tsai-Hill criterion

Tsai-Hill criterion is extended from the distortional energy criterion of von-Mises to anisotropic materials. According to this criterion, the general equation is written as:

$$(G+H)\sigma_1^2 + (F+H)\sigma_2^2 + (F+G)\sigma_3^2 - 2H\sigma_1\sigma_2 - 2G\sigma_1\sigma_3 - 2F\sigma_2\sigma_3 + 2L\sigma_4^2 + 2M\sigma_5^2 + 2N\sigma_6^2 = 1 \tag{8}$$

where F, G, H, L, M, and N are the material strength parameters. For the plane stress in 1–2 plane of a unidirectional lamina with fiber in the two direction, $\sigma_3 = \tau_{13} = \tau_{23} = 0$. Eq. (8) was reduced and written as:

$$\left(\frac{\sigma_1}{S_1}\right)^2 - \frac{\sigma_1\sigma_2}{{S_2}^2} + \left(\frac{\sigma_2}{S_2}\right)^2 + \left(\frac{\tau_{12}}{S_{12}}\right)^2 = 1 \tag{9}$$

Then, we applied Tsai-Hill criterion for the definition of risky areas in failure on the specimen. The stresses at each element are influenced by the interaction between elements. Especially, as mentioned later, σ_2 and τ_{12} were the dominant stress components, so in this study the reduced Tsai-Hill criterion was used as shown in the following: where, S_1 is the transverse strength of the lamina, S_2 is the tensile strength along the fiber axis, and S_{12} is the shear strength. The strength values are given as S_1 = 6.44 MPa, S_2 = 232 MPa, which were obtained by normalizing the SLM experimental values to the fiber volume fraction of 0.70. S_{12} was estimated as a double value of S_1 referring to the data of conventional fibrous composites [22].

The values of Tsai-Hill criterion vary between 0 and 1. When the value tends to approach 0, in general, this location is interpreted as a nonrisky area. In contrast, when it tends to approach 1, this location is recognized as a risky area.

2.6.2. Maximum stress criterion

Maximum stress criterion is given on the assumption that, when the ratio of stress to strength achieves to 1, the failure occurs. For this criterion, we used the longitudinal, transverse strength, and shear strength to predict the risky areas on specimens. Maximum stress criterion was hereinafter denoted as MS. When the MS trends to 1, this is the risky point on the specimen. In contract, MS trends to 0 when the value on the specimen is not the risky point. The MS is described as the below equation.

$$\frac{\sigma_1}{S_1} = 1, \frac{\sigma_2}{S_2} = 1, \text{ and } \frac{\tau_{12}}{S_{12}} = 1 \tag{10}$$

where, S_1, S_2, and S_{12} are transverse strength, longitudinal strength, and shear strength, respectively.

3. Results and discussion

3.1. Tensile test results

Fiber orientation angles and tensile properties of SLM and DM are shown in **Table 2**. The results show that tensile strengths of DM specimens accompanied with the fiber waviness are lower than those of SLM. Young's moduli of DM are also lower. It should be noted that the fiber volume fraction of DM specimens are lower in whole than that of SLM. This is attributed to the fact that the fibers cannot be packed compactly, as compared to SLM specimens, because of irregular fiber waviness. However, the lower volume fraction does not necessarily cause lower tensile strength of DM specimens. Here, we estimate the tensile strength of SLM specimen at 61%, the average fiber volume fraction, using $\sigma_c' = (V_f'/V_f)\sigma_c = (0.61/0.72) \times 238$, which is the lower bound of the law of mixture. Where, σ_c is the composite's tensile strength, V_f is the fiber volume fraction, and a symbol "dash" means a predicted value, such that σ_c' is a value at the fiber volume fraction V_f' predicted from σ_c. The calculated tensile strength was 202 MPa. This value is clearly higher than 175 MPa, the average strength of DM specimens, despite of the value derived from the lower bound. It is considered that, therefore, the waviness is a major factor to reduce the tensile properties in strength of the sliver-based natural fiber composite, whereas several low V_f specimens show relatively large strengths, as mentioned above, and therefore the effect of irregular fiber waviness is needed to be discussed with unified V_f.

3.2. Angle distribution and analytical results of special autocorrelation

In order to make contour maps of the fiber orientation angle distribution, each measured angle was assigned to the center point of each segment. **Figure 5(a)** and **(b)** show examples of the contour color maps. The blue (upper right portion in **5(a)**) and red (center portion slightly to

Production method	Specimens						Tensile strength (MPa)	Young's modulus (GPa)
	Sample no.	Fiber volume fraction	Side A (lower angle)		Side B (higher angle)			
			Avg. angle (°)	S.D. of angles (°)	Avg. angle (°)	S.D. of angles (°)		
SLM*	—	0.72	0	—	0	—	238	40.5
DM	<1>	0.55	1.99	3.54	3.30	4.28	132	22.7
	<2>	0.55	2.62	5.22	4.19	4.03	224	26.7
	<3>	0.55	5.14	4.06	5.55	3.18	158	29.6
	<4>	0.55	3.05	3.22	8.76	4.18	211	27.6
	<5>	0.65	1.74	3.73	2.85	2.66	158	23.3
	<6>	0.65	2.10	2.62	3.07	3.48	203	26.4
	<7>	0.65	1.61	2.33	2.20	2.32	153	27.5
	<8>	0.65	2.08	3.47	3.76	2.95	170	28.0
	<9>	0.65	1.45	3.72	5.26	4.77	173	26.8
	<10>	0.65	0.76	3.50	4.55	3.90	168	28.8
	Avg.	0.61	2.35	3.50	4.35	3.60	175	26.8

*The number of SLM specimens was seven, and their average values are shown.

Table 2. Fiber orientation angles and mechanical properties of flax sliver-reinforced composite laminates [17].

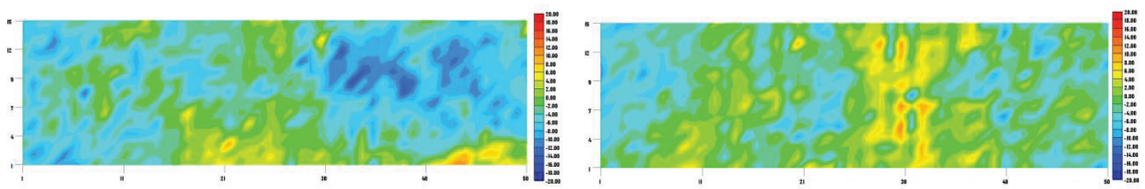

(a) (b)

Figure 5. Contour map of fiber orientation angle distribution. (a) Specimen 2A (avg. angle: 4.19°, standard deviation: 4.03°) and (b) specimen 5A (avg. angle: 4.55°, standard deviation: 3.90°).

the right in **5(b)**) color areas show the high angle on the negative and positive sides respectively on specimens 2A and 5A, of which the fiber orientation angles vary with approximately 4.0 degree standard deviation. Such contour mapping results and statistical aspect mean that the fiber waviness occurs locally and randomly.

Figure 6(a) and **(b)** shows typical examples of analytical results of LM-*I*. As shown in both the figures, positive LM-*I* areas higher than 0.5 are locally distributed with agglomeration of about 5–10 mm scale, whereas several negative LM-*I* areas are dispersed with a smaller scale. In comparison with **Figure 5**, it is recognized that Specimen 5A of **Figure 6(b)** shows quite a similar distribution. Specimen 2A of **Figure 6(a)** shows that, on the other hand, both positive and negative orientation angles are evaluated with similar color levels. In other words, LM-*I* is

http://dx.doi.org/10.5772/intechopen.70905

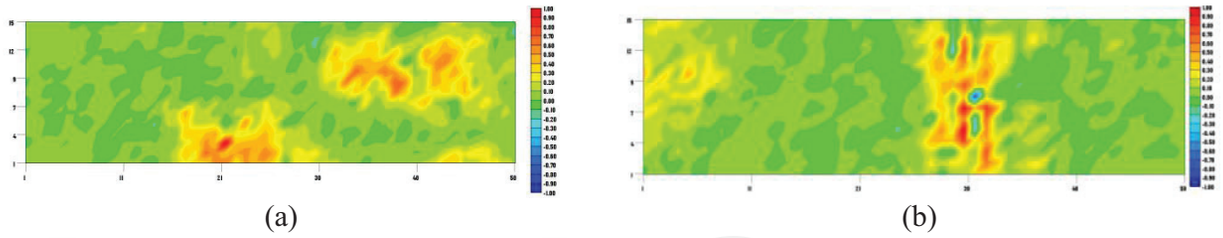

Figure 6. Contour maps of LM-*I* distribution. (a) Specimen 2A and (b) specimen 5A.

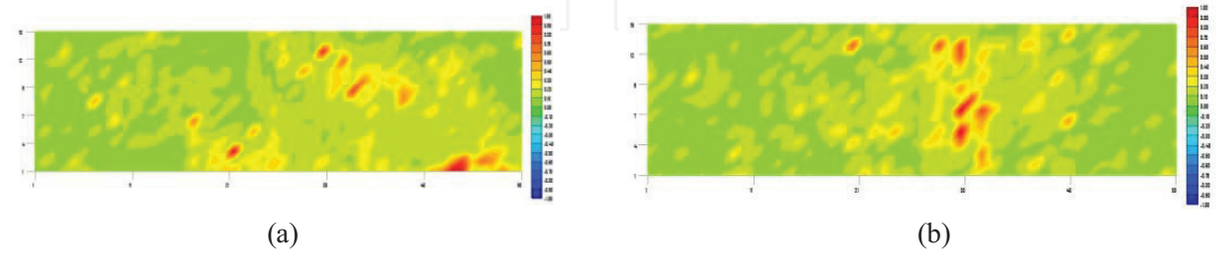

Figure 7. Contour maps of LG-*c* distribution. (a) Specimen 2A and (b) specimen 5A.

characterized by giving an even evaluation, irrespective of the difference between positive and negative angles. We consider, the intensity and scale of such disorders in fiber orientation is related with the tensile strength to some degree.

Figure 7(a) and **(b)** shows typical examples of analytical results of LG-*c*. In these figures, the range from −1 to 1 is intentionally employed to compare them with LM-*I* distribution. As shown in the both figures, LG-*c* areas higher than 0.5 are locally dispersed with about 1–3 mm scale, quite smaller than LM-*I*, whereas major parts of the specimens are occupied by low LG-*c* values. Thus, LG-*c* is a measure accompanied with locally smaller scale.

3.3. Threshold levels of LM-*I* and LG-*c* values: definition of area ratio

In this section, we tried to quantify the results of the above spatial analyses by using the concept of "area ratio" characterized by threshold levels. If the area ratios are well correlated with tensile strength data, the strength could be estimated from the fiber orientation angle distribution measured in advance. In this quantification, we used two imaging programs; first is "Graph R221," which was used for plotting a contour map, and the next is "Azo R235," which was used for calculation of area ratio.

For instance, when we choose temporarily threshold levels higher than 0.3 or less than −0.1, the corresponding LM-*I* areas can be obtained, as shown in black areas of **Figure 8(a)**, **(b)**. In these cases, the area ratios of specimens were calculated as 12.6% (positive side = 11.1% and negative side = 1.5%) and 9.1% (positive side = 6.8% and negative side = 2.3%) for the specimens 2A and 5A, respectively. In **Figure 9(a)**, **(b)**, the black areas of LG-*c* are higher than 0.2 were selected. The area ratios of specimens were calculated as 16.5 and 13.5% for specimens 2A and 5A, respectively.

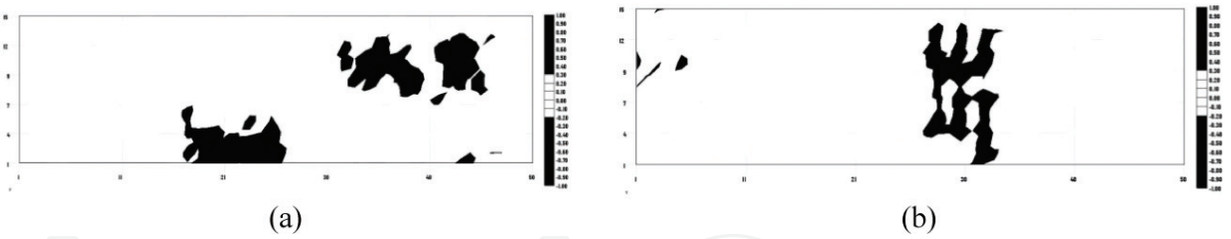

Figure 8. Binary images of Local Moran's *I* distribution: (a) Specimen 2A and (b) specimen 5A (threshold levels: positive LM-*I* = 0.30 and negative LM-*I* = −0.10).

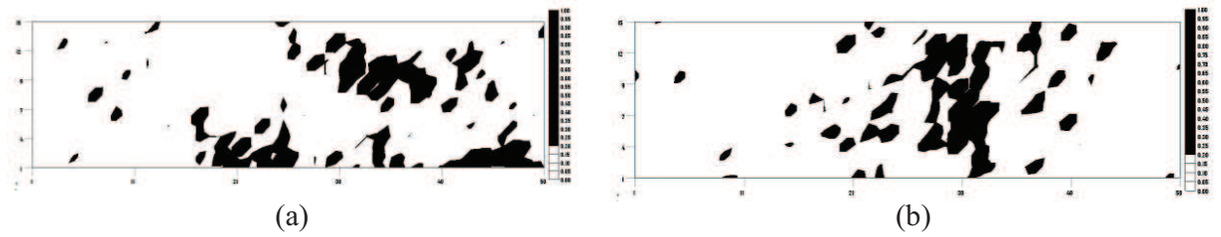

Figure 9. Binary images of local Geary's *c* distribution: (a) Specimen 2A and (b) specimen 5A (threshold level: LG-*c* = 0.20).

Here, we consider the change in area ratio with change in threshold level. Regarding LM-*I*, we take an account of the threshold levels of negative value with a relatively wide range, similarly to that of positive values. This is because the segments with negative LM-*I* values have a possibility of causing premature damage in shear, although these are not so major. We consider, if appropriate threshold levels are given, there is an optimal area ratio at each specimen, which is well correlated with tensile strength. In other words, the ratio of segments suffering damage during tensile loading should be related closely with the area ratio. In the next segment, thus, the relation between area ratio and tensile strength is investigated.

3.4. Relation between area ratio and tensile strength

To investigate the correlation between the area ratio and tensile strength, normalized tensile strength data were plotted as a function of area ratio, as shown in **Figures 10** and **11**. In these plots, each tensile strength value was normalized by dividing the measured strength by the fiber volume fraction V_f and then multiplying it by 0.72, which is V_f of SLM specimen. In **Figure 10**, it is confirmed that the normalized strength is correlated with the area ratio to some extent. The correlation coefficients of LM-*I* were respectively calculated as −0.44 and −0.65 when setting threshold levels at LM-*I* > 0.6 or LM-*I* < −0.1 in **Figure 10(a)** and LM-*I* > 0.8 or LM-*I* < −0.1 in **Figure 10(b)**. The value of −0.65 is not so strong but presents an intermediate strong correlation. This means, if many segments in a specimen are distributed with LM-*I* values higher or lower than the above threshold levels, its tensile strength tends to be lowered. It also means that a rough value of tensile strength can be estimated through the least-squares regression line between area ratio and tensile strength.

http://dx.doi.org/10.5772/intechopen.70905

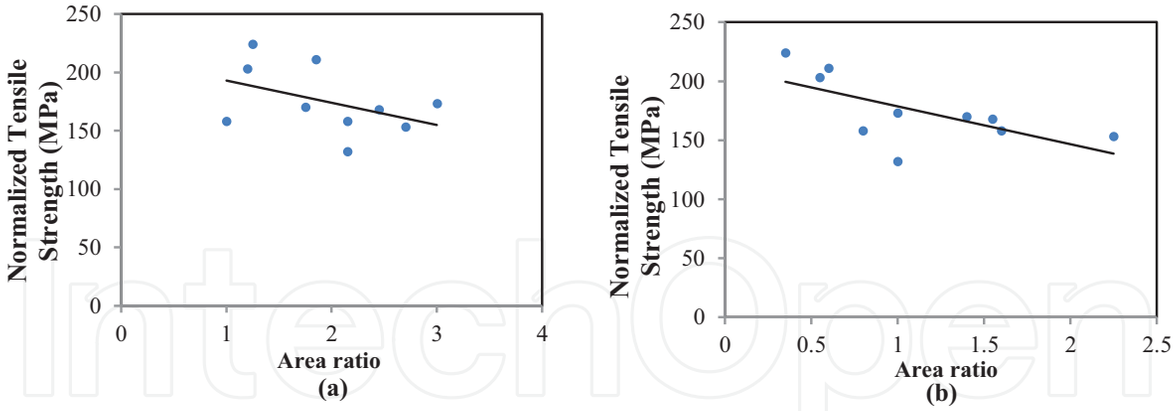

Figure 10. LM-*I* area ratio dependence on normal tensile strength. (a) Threshold levels: LM-*I* > 0.6 or LM-*I* < −0.1 and (b) threshold levels: LM-*I* > 0.8 or LM-*I* < −0.1.

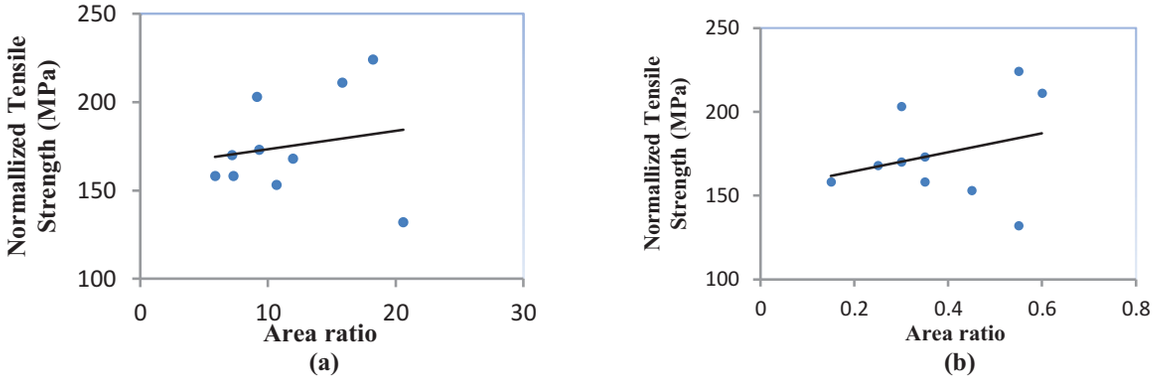

Figure 11. LG-*c* area ratio dependence on normal tensile strength. (a) Threshold levels: LG-*c* > 0.2 and (b) threshold levels: LG-*c* > 0.5.

In contrast, the LG-*c* area ratio plots are not so correlated with tensile strength data, as shown in **Figure 11(a)** and **(b)**. The correlation coefficients between the area ratio and tensile strength were obtained as 0.18 and 0.29, when setting threshold levels at 0.2 and 0.5, respectively. The both values of 0.18 and 0.29 obviously signify weak correlation. This result implies that the values of 0.2 and 0.5 are inappropriate as a threshold level, or that LG-*c* is a measure not to match correlation with tensile strength.

Figure 12(a) shows the change in correlation coefficient with change in positive threshold level of LM-*I*. In this case, the negative threshold level was fixed at −0.1. It is found that the correlation coefficient decreases gradually approximately from 0.25, and shows the lowest value around 0.70, which is approximately −0.80, the highest negative coefficient meaning a strong correlation. The correlation coefficient is also sensitive for the change in negative threshold level, as shown in **Figure 12(b)**. Three positive threshold levels, 0.69, 0.75, and 0.77, were chosen for simplicity. It is confirmed that the optimal threshold levels of LM-*I* are 0.69 at the positive level and −0.10 at the negative level. These optimal levels brought the correlation coefficient of −0.832, from which it is concluded that LM-*I* area ratio yields a strong correlation

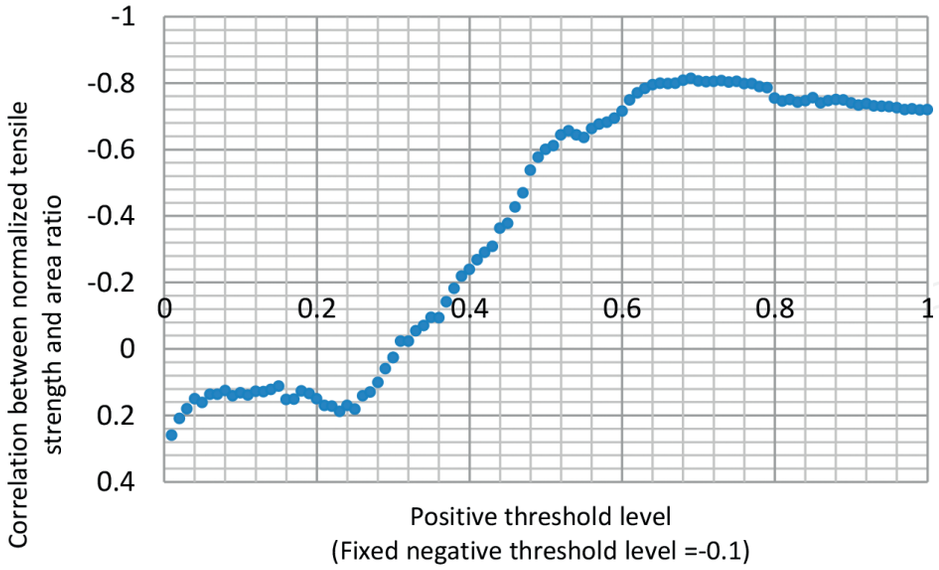

(a)

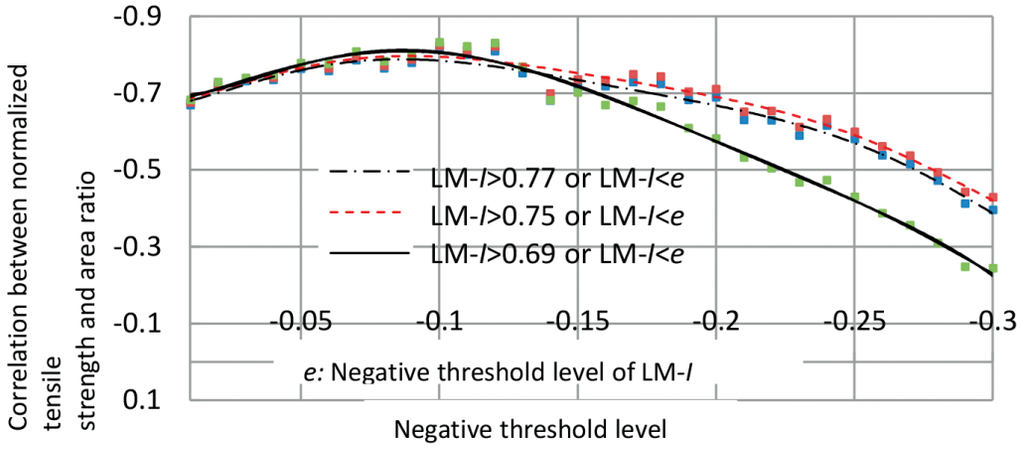

(b)

Figure 12. Correlation coefficients between LM-*I* area ratio and normalized tensile strength. (a) Correlation coefficient vs. positive threshold level. (b) Correlation coefficient vs. negative threshold level.

with tensile strength. In other words, tensile strength can be estimated to some degree through the least-squares regression line when setting the optimal threshold levels of LM-*I*. It is also expected that the present procedure is applied as an effective screening method extracting low quality pre-pregs at quality inspection.

Figure 13 shows the relation between correlation coefficient and threshold level of LG-*c*. Although the coefficient varies with change in the threshold level of LG-*c*, the highest coefficient is only −0.14 at threshold level of 0.36. This coefficient value is quite a weak correlation, and therefore it is concluded that LG-*c* area ratio is not a parameter to match correlation with tensile strength.

http://dx.doi.org/10.5772/intechopen.70905

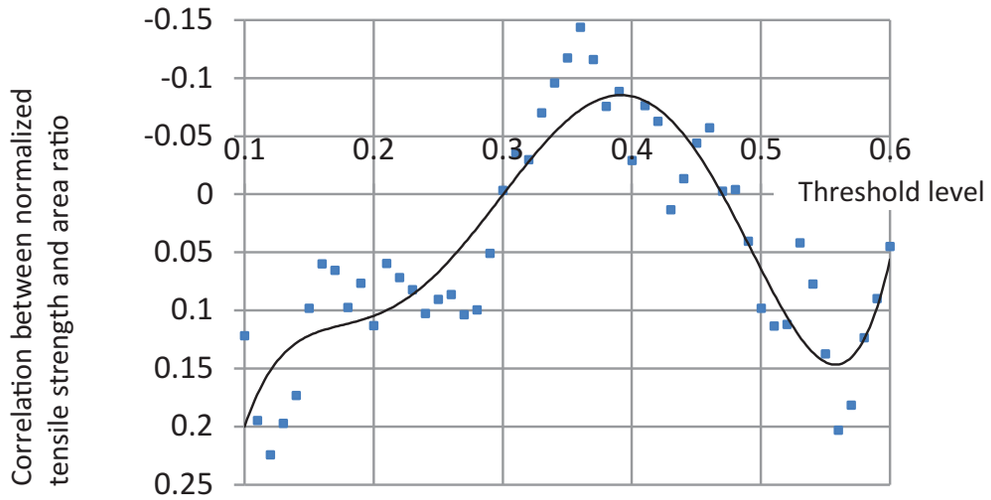

Figure 13. Correlation coefficients between LG-*c* area ratio and normalized tensile strength vs. threshold level.

3.5. Normalized stress distributions and maximum stress criterion

Figure 14 shows typical computed stress distributions. **Figure 14(a)** and **(b)** shows σ_x and σ_y contour maps, respectively, which were divided by the maximum value of all normal stress components. σ_z contour map is omitted in **Figure 14** because it is quite the same as σ_x contour map. **Figure 14(c–e)** are τ_{xy}, τ_{yz}, and τ_{zx} contour maps, respectively, which are divided by the

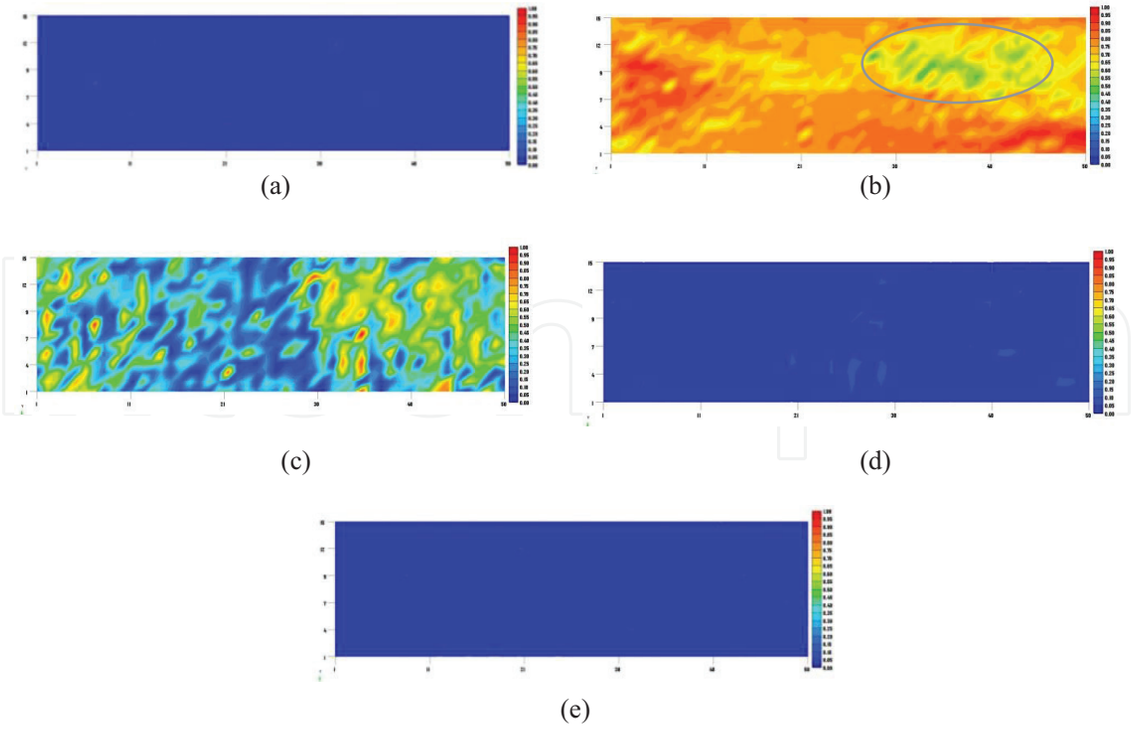

Figure 14. Contour map of normalized stress distributions (Specimen 2A). (a) Contour map of σ_x distribution; (b) contour map of σ_y distribution; (c) contour map of τ_{xy} distribution; (d) contour map of τ_{yz} distribution and (e) contour map of τ_{zx} distribution.

maximum value of all shear stress components. The shear stress components were replaced by absolute values. It is proved that σ_y distribution is much larger than σ_x and σ_z, because the specimen is reinforced along the loading axis (y-axis). Regarding the case of shear stress, τ_{xy} distribution working in the plane is also much higher than the others. Shear stress τ_{yz} slightly occurs in the specimen, while τ_{zx} components are negligibly small.

To evaluate the degree of contribution of on-axis stress components to damage occurrence, the maximum stress criterion was used, in which the on-axis stresses, $\sigma_1, \sigma_2, \sigma_3, \tau_{12}, \tau_{23}$, and τ_{31}, were divided by the failure stresses, respectively.

$$\tilde{\sigma}_1 = \frac{\sigma_1}{S_1}, \tilde{\sigma}_2 = \frac{\sigma_2}{S_2}, \tilde{\sigma}_3 = \frac{\sigma_3}{S_1}, \tilde{\tau}_{12} = \frac{\tau_{12}}{S_{12}}, \tilde{\tau}_{23} = \frac{\tau_{23}}{S_{12}}, \text{and } \tilde{\tau}_{31} = \frac{\tau_{31}}{S_{12}} \tag{11}$$

The normalized stresses in Eq. (11) were furthermore unified by dividing them by α (α: the maximum value of $\tilde{\sigma}_1, \tilde{\sigma}_2, \tilde{\sigma}_3, \tilde{\tau}_{12}, \tilde{\tau}_{23}$, and $\tilde{\tau}_{31}$) in order to deal with the maximum as 1.0. Contour map of $\tilde{\sigma}_3$ is again omitted because of the less stress values. In comparison between **Figure 15(a–e)**, the maximum normalized stress was found in **Figure 15(c)**. It means that the damage or failure may occur in $\tilde{\tau}_{12}$, although the area scale is small. The second risky normalized stress was found in $\tilde{\sigma}_2$ of **Figure 15(b)**. $\tilde{\sigma}_1$ in **Figure 15(a)** are still affecting on the specimens but they do not have influence so much. Regarding $\tilde{\tau}_{23}$ and $\tilde{\tau}_{31}$, they are also quite small, and therefore we can neglect them from the fracture criterion. The same tendency was

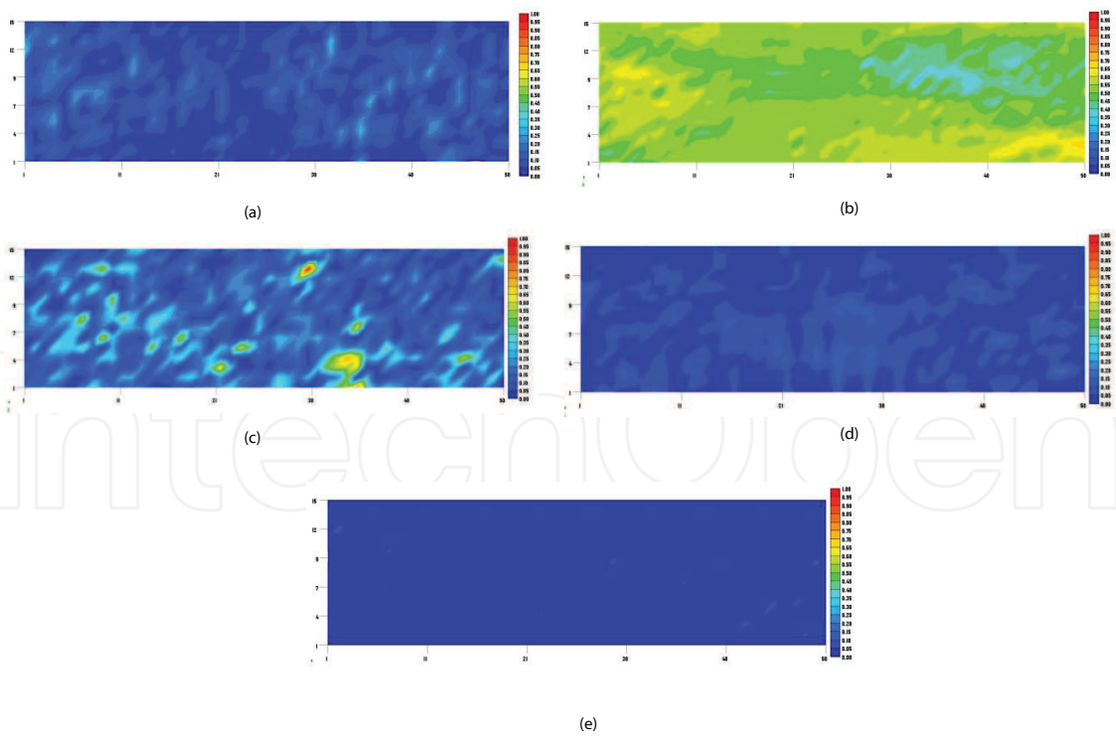

Figure 15. Contour maps of unified normalized stress-distribution based on the maximum stress criterion (Specimen 2A). (a) Contour map of unified $\tilde{\sigma}_1$ distribution; (b) contour map of unified $\tilde{\sigma}_2$ distribution; (c) contour map of unified $\tilde{\tau}_{12}$ distribution; (d) contour map of unified $\tilde{\tau}_{23}$ distribution and (e) contour map of unified $\tilde{\tau}_{31}$ distribution.

also confirmed in the other specimens. Thus, tensile strength of the specimens may be affected by local shear damage mode, according to the maximum stress criterion. But, we should also focus on the possibility of tensile fracture, because the size of the risky area is larger than the shear damage area, as seen from comparison between **Figure 15(b)** and **(c)**.

3.6. Comparison between spatial autocorrelation analyses, maximum stress criterion and Tsai-Hill criterion with the fracture specimen

Figure 16(a) and **(b)** shows the fractured specimen (Sample No.2) and the contour map of Tsai-Hill criterion, respectively. As is seen, the latter resembles **Figure 15(c)**. This means, the obtained result from Tsai-Hill criterion is occupied by in-plane shear stress component. In comparison between **Figure 16(a)** and **(b)**, the both shear fracture portions of the upper and lower sides (see, arrows) in **Figure 16(a)** may be slightly different from those of **Figure 16(b)**, but the locations are quite close. It is considered that, on the other hand, it may be severe to cause the whole fracture from such small damage areas. It also looks in **Figure 16(a)** that tensile fracture occurs between the two shear damage areas. **Figure 16(c)** shows σ_y stress distribution of specimen 2B. It is confirmed that the tensile fracture portion is loaded more largely, whereas σ_y stress distribution of specimen 2A in **Figure 14(b)** is reduced (see both regions surrounded by an ellipse). It is estimated that such an unbalanced σ_y stress distribution between laminae 2A and 2B causes the final tensile fracture. In other specimens, the similar unbalanced σ_y stress distributions were confirmed (it is omitted because of limited space). It is predicted that, thus, although the flax sliver-based composite with irregular fiber waviness may receive some small damages firstly, finally this fractures due to the unbalanced normal stress distribution between laminae.

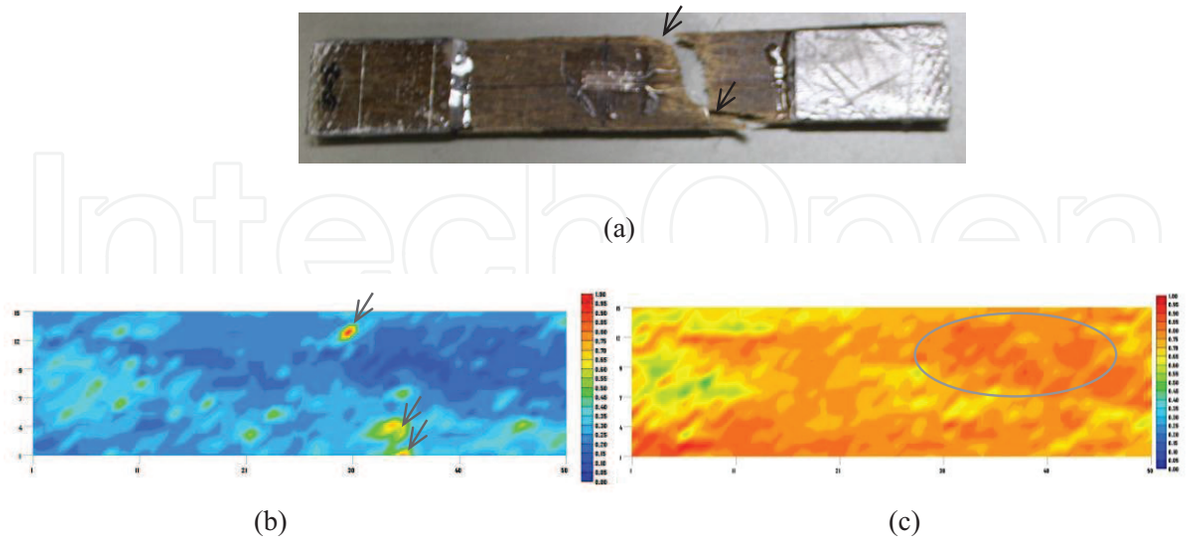

Figure 16. Comparison between fractured specimen, Tsai-Hill criterion and normal stress distribution. (a) Fractured specimen; (b) contour map of Tsai-Hill criterion (specimen 2A) and (c) contour map of σ_y stress distribution (specimen 2B) divided by the same maximum value as (specimen 2A).

4. Conclusions

The effect of irregular fiber waviness on tensile strength of a flax sliver-based biodegradable thermoplastic resin composite laminate was clarified. The fiber orientation angles were measured at fine segments on the both surfaces of the composite specimen. As a first approach, two representative spatial analyses, Local Moran's *I* and Local Geary's *c*, were carried out for the quantification of the fiber waviness. Then, we calculated correlation coefficients between tensile strength and various area ratios obtained by changing the ranges of Local Moran's *I* and Local Geary's *c*. The results showed that Local Moran's *I* was correlated well with tensile strength of the composite specimens when appropriate ranges were selected. On the other hand, Local Geary's *c* was not well correlated with tensile strength. Thus, it is concluded that the analysis method used in this study is an effective tool of predicting roughly the tensile strength of natural fiber-sliver-based composites.

As a next approach, we evaluated stress distributions in the composite specimen using a three-dimensional finite element analysis (3-D FEA) based on the orthotropic theory, in which measured fiber orientation angles were substituted for the finite elements. Results showed that σ_y distribution was much larger than σ_x and σ_z, which means that the specimen is reinforced along the loading axis (*y*-axis) despite of irregular fiber orientation. Regarding the other stresses, in-plane shear stress, τ_{xy}, was much higher than the others. Shear stress τ_{yz} slightly occurred in the specimen, whereas τ_{zx} components were negligibly small. For these results, the maximum stress criterion was firstly applied, in which the on-axis stresses, σ_1, σ_2, σ_3, τ_{12}, τ_{23}, and τ_{31}, (where 1 and 3 are the transverse direction of the fiber axis, and 2 is the fiber axis) were divided by the failure stresses, respectively. As a result, the normalized maximum stress was found on τ_{12} distribution map. It means that a small damage may occur in τ_{12}. The fiber axis stress, σ_2, occupied a relatively large stress area, although the stress itself is smaller than the normalized maximum stress of τ_{12}. Tsai-Hill criterion, was also applied to predict more dangerous damage areas in the composite specimen. These results were compared with fracture paths of the actual specimens. It was estimated that, finally, fracture occurred by enhanced tensile stress occurring in the counterpart of the composite laminate, which was caused by partially off-axial fiber area in a lamina.

Author details

Taweesak Piyatuchsananon[1], Baosheng Ren[2] and Koichi Goda[3]*

*Address all correspondence to: goda@yamaguchi-u-ac.jp

1 Automotive Engineering Department, Siam University, Thailand

2 Department of Mechanical Engineering, University of Jinan, China

3 Department of Mechanical Engineering, Yamaguchi University, Japan

References

[1] Compositesworld.com, The Making of Carbon Fiber: Composites World. 2015. [Online]. Available: http://www.compositesworld.com/articles/the-making-of-carbon-fiber

[2] Peijs T. Composites for recyclability. Materials Today. 2003;**6**:30-35

[3] López FA, Martín MI, García-Díaz I, Rodríguez O, Alguacil FJ, Romero M. Recycling of glass fibers from fiberglass polyester waste composite for the manufacture of glass-ceramic materials. Journal of Environmental Protection. 2012;**3**:740-747

[4] Duan H, Jia W, Li J. The recycling of comminuted glass-fiber-reinforced resin from electronic waste. Journal of the Air & Waste Management Association. 2010;**60**:532-539

[5] Liu L, Yu J, Cheng L, Yang X. Biodegradability of poly(butylene succinate) (PBS) composite reinforced with jute fibre. Polymer Degradation and Stability. 2009;**94**:90-94

[6] Alix S, Marais S, Morvan C, Lebrun L. Biocomposite materials from flax plants: Preparation and properties. Composites: Part A. 2008;**39**:1793-1801

[7] Lodha P, Netravali AN. Characterization of stearic acid modified soy protein isolate resin and ramie fiber reinforced 'green' composites. Composites Science and Technology. 2005;**65**:1211-1225

[8] Serizawa S, Inoue K, Iji M. Kenaf-fiber-reinforced poly(lactic acid) used for electronic products. Journal of Applied Polymer Science. 2006;**100**:618-624

[9] Gomes A, Matsuo T, Goda K, Ohgi J. Development and effect of alkali treatment on tensile properties of curaua fiber green composites. Composites. Part A. 2007;**38**:1811-1820

[10] Goda K, Cao Y. Research and development of fully green composites reinforced with natural fibers. Journal of Solid Mechanics and Materials Engineering. 2007;**1**:1073-1084

[11] Hsiao HM, Daniel IM. Elastic properties of composites with fiber waviness. Composites: Part A. 1996;**27**:931-941

[12] Karami G, Garnich M. Effective moduli and failure considerations for composites with periodic fiber waviness. Composite Structures. 2005;**67**:461-475

[13] Anumandla V, Gibson RF. A comprehensive closed form micromechanics model for estimating the elastic modulus of nanotube-reinforced composites. Composites: Part A. 2006;**37**:2178-2185

[14] Allison BD, Evans JL. Effect of fiber waviness on the bending behavior of S-glass/epoxy composites. Materials and Design. 2012;**36**:316-322

[15] Bogetti TA, Gillespie JW JR, Lamontia MA. The influence of ply waviness with nonlinear shear on the stiffness and strength reduction of composite laminates. Journal of Thermoplastic Composite Materials. 1994;**7**:76-90

[16] Ren B, Noda J, Goda K. Effects of fiber orientation angles and fluctuation on the stiffness and strength of sliver-based green composites, zairyo. Japan: Journal of the Society of Materials Science; 2010;**59**:567-574

[17] Ren B, Mizue T, Goda K, Noda J. Effects of fluctuation of fibre orientation on tensile properties of flax sliver-reinforced green composites. Composite Structures. 2012;**94**: 3457-3464

[18] Fortin M-J, Dale M. Spatial Analysis. New York: Cambridge University Press; 2005. p. 111

[19] Tsai C-H, Zhang C, Jack DA, Liang R, Wang B. The effect of inclusion waviness and waviness distribution on elastic properties of fiber-reinforced composites. Composites: Part B. 2011;**42**:62-70

[20] Jones RM. Mechanics of Composite Materials. 2nd ed. Philadelphia: CRC Press; 1999. p. 117

[21] Younes R, Hallal A, Fardoun F, Chehade FH. Comparative review study on elastic properties modeling for unidirectional composite materials. In: Hu N, editor. Composites and Their Properties. Croatia: Intech; 2012. p. 391-408

[22] Matthews FL, Rawlings RD. Composite Materials: Engineering and Science. Cambridge: Woodhead Publishing; 1999. p. 270